Available online at www.sciencedirect.com
ScienceDirect
Journal of Catalysis 250 (2007) 12–18
JOURNAL OF CATALYSIS
www.elsevier.com/locate/jcat

Photocatalytic performance of α-, β-, and γ-Ga_2O_3 for the destruction of volatile aromatic pollutants in air

Yidong Hou, Ling Wu, Xinchen Wang, Zhengxin Ding, Zhaohui Li, Xianzhi Fu *

Research Institute of Photocatalysis, State Key Laboratory Breeding Base of Photocatalysis, Fuzhou University, Fuzhou 350002, PR China

Received 5 March 2007; revised 18 May 2007; accepted 25 May 2007

Available online 27 June 2007

Abstract

Three polymorphs of Ga_2O_3 (α-, β-, and γ-Ga_2O_3) were prepared, and their photocatalytic activities were evaluated by the decomposition of volatile aromatic compounds (e.g., benzene, toluene, and ethylbenzene) in dry air stream under UV light illumination at room temperature. It was found that the Ga_2O_3 catalysts exhibited much higher photocatalytic activity than commercial TiO_2. The photocatalytic activities of the Ga_2O_3 polymorphs were strongly influenced by their crystal structure, and their specific activities decreased in the following order: β-Ga_2O_3 > α-Ga_2O_3 > γ-Ga_2O_3. The reasons for the differences in photocatalytic activity of the Ga_2O_3 polymorphs are discussed in terms of crystallinity, geometric structure, and electronic properties of the polymorphs.

Keywords: Photocatalysis; Ga_2O_3; Geometric structure; Photoluminescence

1. Introduction

Volatile organic compounds (VOCs) are an important class of air pollutants originating from industrial and urban sources. Some VOCs (e.g., methane, chlorofluorocarbons) are "greenhouse effect" gases causing global warming, and others (e.g., aromatic compounds) can lead to serious and devastating environmental and health problems. For example, workers exposed to benzene fumes have an increased risk of leukemia and bone-marrow toxicity [1]. Benzene is also considered to have carcinogenic, mutagenic, and teratogenic effects on the human body.

Several advanced oxidation technologies for the removal of various pollutants have been studied, among which photocatalytic oxidation over TiO_2 appears to be very attractive [2,3]. Irradiation of TiO_2 with UV or near-UV light induces the production of highly active species such as $O_2^-\bullet$, $HO_2\bullet$, $OH\bullet$, and so on [4], initiating redox reactions that decompose VOCs. The photocatalytic process can be conducted at room temperature and is cost-effective, efficient, and environmentally benign. Many diluted VOCs, such as formaldehyde, acetone, benzene, and toluene in both gas and liquid phases, have been decomposed over a TiO_2 photocatalyst. In some cases, complete oxidation of organic compounds has been reported. However, TiO_2 photocatalyst is often deactivated, especially for the oxidation of aromatics in dry air stream, due to the deposition of less-reactive byproducts (probably polymeric products) on the catalyst surface [5,6]. Adding a sufficient amount of H_2O vapor into the reaction system has been done to suppress carbon deposition and thus improve the durability of the photocatalyst [7,8]. Loading of a noble metal (Pt, Pd, or Rh) on TiO_2 is a common approach to enhancing the photo-oxidation and mineralization of aromatic compounds in humidified air stream [8–11]. Although Rh/TiO_2 has been shown to be the best of the metal-modified TiO_2 photocatalysts, it still suffers from gradual deactivation, attributed mainly to the oxidation of Rh nanoparticles [11]. It also has been found that introduction of trace amounts of H_2 into the photochemical reaction system significantly increased the activity of Pt/TiO_2 for benzene photocatalytic oxidation by two orders of magnitude [12]. In this photoreaction system, all of the benzene in dry air stream can be mineralized completely and quickly to CO_2 and H_2O, and no catalyst deactivation is observed during prolonged operation. But realizing such a complicated system for air purification is not technically easy, due to safety concerns. Therefore, it

* Corresponding author. Fax: +86 591 83738608.
E-mail address: xzfu@fzu.edu.cn (X. Fu).

0021-9517/$ – see front matter
doi:10.1016/j.jcat.2007.05.012

is desirable to develop alternative approaches to improve the system's efficiency for the photocatalytic removal of aromatic compounds. In this regard, the development of novel non-TiO_2-based materials as efficient photocatalysts has been explored. Recently, we found that pure β-Ga_2O_3 was highly photoactive for the mineralization of gaseous benzene and its derivatives (e.g., toluene and ethylbenzene) to CO_2 and H_2O at room temperature without the problem of catalyst deactivation [13].

The activity of a photocatalyst is known to be strongly related to its physicochemical properties, particularly its crystalline structure [14–17]. For example, the photocatalytic activity of anatase TiO_2 is much higher than that of rutile TiO_2 [15]. This has been attributed to the differences in the rate of recombination, adsorptive affinity, or band gap among the polymorphs [15,16]. Ga_2O_3 has five polymorphs, designated as α-, β-, γ-, δ-, and ε-Ga_2O_3 [18]. Among these polymorphs, α-Ga_2O_3 is rhombohedral, β-Ga_2O_3 is monoclinic, and γ-Ga_2O_3 is cubic. These different crystal structures significantly influence the surface properties of Ga_2O_3 [19–21], accounting for the variation in catalytic activity among the polymorphs [19].

To the best of our knowledge, the literature contains no reports comparing the photocatalytic activity and crystal structure of Ga_2O_3. In the present work, three polymorphs of Ga_2O_3 (α-, β-, and γ-Ga_2O_3) were prepared and characterized by powder X-ray diffraction (XRD), N_2-sorption, Raman spectroscopy, UV–vis diffuse reflectance spectroscopy, and photoluminescence (PL) spectroscopy, and their photocatalytic performance for the degradation of aromatic compounds was compared based on their physicochemical properties and crystal structures.

2. Experimental

2.1. Catalyst preparation

To prepare α-Ga_2O_3, aqueous ammonia solution (5 wt%) was slowly added to a gallium nitrate solution (10 wt%) under continuous stirring until the pH value of the solution reached ca. 8. The resulting precipitate was filtered, washed with water, and vacuum-dried in a desiccator. The solid thus obtained was calcined for 5 h at 773 K to yield α-Ga_2O_3. For the preparation of γ-Ga_2O_3 and β-Ga_2O_3, first gallium nitrate was dissolved in ethanol (approximately 3 g of the salt in 50 ml of the solvent), and then an ethanol solution of aqueous ammonia (volume ratio of ethanol/aqueous ammonia = 1) was added slowly under continuous stirring at room temperature until no further precipitate was formed [22]. The resultant precipitate was filtered, washed with ethanol, and vacuum-dried in a desiccator. Then the obtained solid was calcined at 773 and 873 K for 5 h to produce γ-Ga_2O_3 and β-Ga_2O_3, respectively.

2.2. Characterization

Powder X-ray diffraction (XRD) data were collected using a Bruker D8 Advance X-ray diffractometer (Cu$K\alpha_1$ irradiation, $\lambda = 1.5406$ Å). Raman spectra were obtained using a Perkin–Elmer Spectrum 2000 R NIR FT-Raman spectrophotometer, equipped with a Nd/YAG laser and a InGaAs detector. UV–vis diffuse reflectance spectra were obtained using a Varian Cary 500 UV–vis–NIR spectrometer and were converted from reflection to absorption by the Kubelka–Munk method. The specific surface area of the samples was measured by nitrogen sorption at 77 K on OMNISORP100CX instrument and calculated by the BET method. PL spectra were obtained using an Edinburgh Analytical Instruments FL/FSTCSPC920 coupled with a time-correlated single-photo counting system.

2.3. Photocatalytic activity test

Photocatalytic experiments were conducted using a fixed-bed tubular quartz reactor operated in a single-pass mode. The catalyst (0.3 g) was loaded into the reactor surrounded by four 4-W UV lamps with a wavelength centered at 254 nm (Philips, TUV 4W/G4 T5). To eliminate the effect of humidity and compare the photocatalytic performance of Ga_2O_3 and TiO_2 under the same conditions, the photocatalytic reactions were performed under dry air conditions. Zero-air-balanced benzene (450 ppm), toluene (450 ppm), or ethylbenzene (350 ppm) was used to afford a reactant stream. The flow rate of reactant mixture was kept at 20 ml min^{-1}. Simultaneous determination of hydrocarbon and CO_2 concentrations was performed with an online gas chromatograph (HP6890) equipped with a flame ionization detector, a thermal conductivity detector, and a Porapak R column. The original concentration of CO_2 in the reactant stream was 0 ppm. The reaction temperature of the photocatalytic system was controlled at $27 \pm 1\,^{\circ}C$ by an air-cooling system. All photocatalytic experiments were carried out only after the equilibrium adsorption of aromatics and steady state of reaction were achieved.

3. Results

3.1. XRD and Raman spectroscopy

Fig. 1 shows the XRD patterns of the Ga_2O_3 polymorphs. The diffraction peaks for each sample can be indexed as a single crystalline phase, namely rhombohedral for α-Ga_2O_3, base-centered monoclinic for β-Ga_2O_3, and face-centered cubic for γ-Ga_2O_3 [18,22]. The sharp diffraction peaks shown in the patterns of α-Ga_2O_3 and β-Ga_2O_3 samples indicate that the two samples have relatively high crystallinity. The broad and weak peaks of the γ-Ga_2O_3 sample may be caused by its low crystallinity. The crystal size of the Ga_2O_3 polymorphs is estimated by Scherrer's equation. These results, along with other physicochemical parameters obtained from the N_2-sorption tests, are shown in Table 1.

To overcome the limitations of XRD in dealing with the short-range structures of materials, we used Raman spectroscopy in this study because of its high sensitivity in determining the local order. The Raman spectra of the Ga_2O_3 polymorphs are shown in Fig. 2. For α-Ga_2O_3, Raman peaks at 216, 284, 430, 573, and 689 cm^{-1} can be seen, in agreement with the literature [23]. In the Raman spectrum of β-Ga_2O_3, peaks at 200, 318, 349, 417, 474, 629, 653, and 766 cm^{-1}

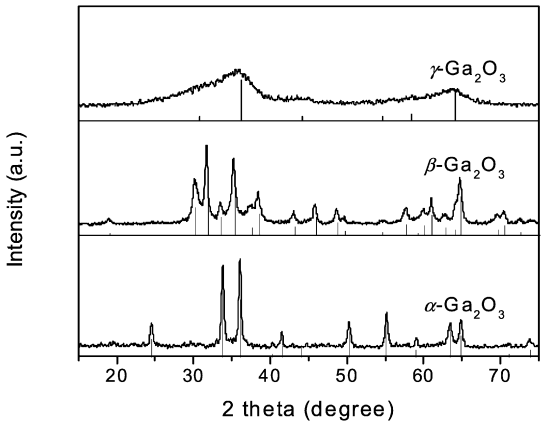

Fig. 1. XRD patterns of the Ga_2O_3 polymorphs.

Table 1
Summary of the physicochemical properties of the Ga_2O_3 polymorphs

Sample	Crystal size[a] (nm)	S_{BET}[b] ($m^2\ g^{-1}$)	Total pore volume[c] ($cm^3\ g^{-1}$)	Mean pore size[d] (nm)
α-Ga_2O_3	23	58	0.15	3.0
β-Ga_2O_3	19	80	0.26	7.3
γ-Ga_2O_3	3.0	135	0.34	3.5

[a] Determined according to the Scherrer equation using the fwhm of α-Ga_2O_3 (110), β-Ga_2O_3 (111), and γ-Ga_2O_3 (311) peaks, respectively.
[b] Calculated from the linear part of the BET plot ($P/P_0 = 0.05$–0.3).
[c] Taken from the volume of N_2 desorbed at about $P/P_0 = 0.97$.
[d] Estimated using the desorption branch of the isotherm and the Barrett–Joyner–Halenda (BJH) formula.

are observed. These peaks are characteristic of monoclinic Ga_2O_3 [23]. Only several weak, broad bands attributable to the bending and stretching of the Ga–O bond can be seen in the Raman spectrum of γ-Ga_2O_3. This confirms the low crystallinity of γ-Ga_2O_3. The Raman results are in good agreement with the XRD analyses. We also attempted to prepare δ-Ga_2O_3 and ε-Ga_2O_3 according to the literature [18,19] but found that we could not identify their crystal phase unambiguously by XRD and Raman analyses; therefore, we do not include these photocatalytic tests in the present work.

3.2. UV–vis diffuse reflectance spectroscopy

Fig. 3 shows UV–vis diffuse reflectance spectra of the Ga_2O_3 polymorphs. For all samples, light absorption starts at around 300 nm and increases steeply at around 270 nm. This is due to the absorption of light caused by the excitation of electrons from the valence band to the conduction band of Ga_2O_3. The inset profile shows that the plots of $(ahv)^2$ versus the energy of light (hv) afford band-gap energies of 4.56, 4.70, and 4.67 eV for α-, β-, and γ-Ga_2O_3, respectively. The band-gap energy values of Ga_2O_3 materials are in the range (4.2–4.9 eV) reported by other researchers [24–26]. The slight difference in the band gap of the Ga_2O_3 polymorphs might be caused by the difference in their lattice structures. This structural difference often leads to different electronic band structures in metal oxides [27,28].

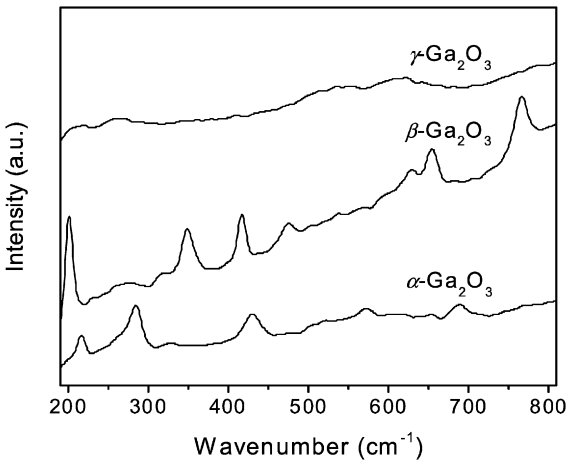

Fig. 2. Raman spectra of the Ga_2O_3 polymorphs.

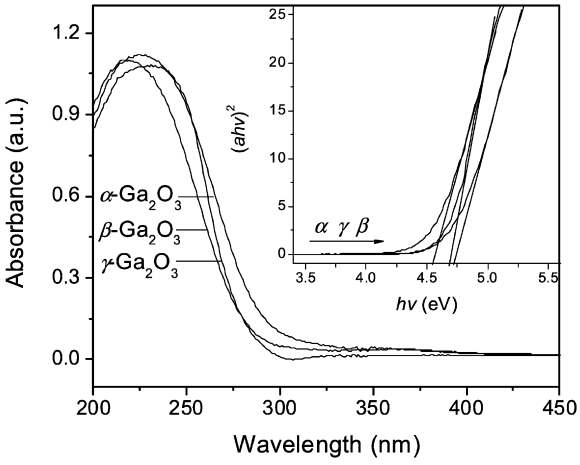

Fig. 3. UV–vis diffuse reflectance spectra of the Ga_2O_3 polymorphs, the inset shows the plots of $(ahv)^2$ versus the energy of light (hv).

3.3. PL spectroscopy

The PL spectra of the Ga_2O_3 polymorphs measured at 77 K are shown in Fig. 4. All samples have a broad emission band at around 490 nm (Fig. 4a). This is attributed to the recombination of an electron on a donor formed by an oxygen vacancy and a hole on an acceptor by either a gallium vacancy or gallium–oxygen vacancy pairs [29–31]. We examined the decays of PL transition centered on 490 nm when the samples were excited at 254 nm. Fig. 4b clearly shows that the PL decay in γ-Ga_2O_3 is faster compared with those in α-Ga_2O_3 and β-Ga_2O_3. Table 2 summarizes the PL decay parameters recovered by the exponential analysis. As shown in Table 2, the PL lifetime of the Ga_2O_3 is on the order of microseconds, and the PL lifetime of three samples decreases in the following order: β-$Ga_2O_3 > \alpha$-$Ga_2O_3 > \gamma$-Ga_2O_3. The amplitudes of the three decay components are different among the Ga_2O_3 polymorphs. The amplitude of the middle decay component locates around 40%. In cases of longer decay component amplitudes, it varies from 16% in γ-Ga_2O_3 to 38% in β-Ga_2O_3. For the shorter decay component, amplitude varies from 38% in γ-Ga_2O_3 to 26% in β-Ga_2O_3.

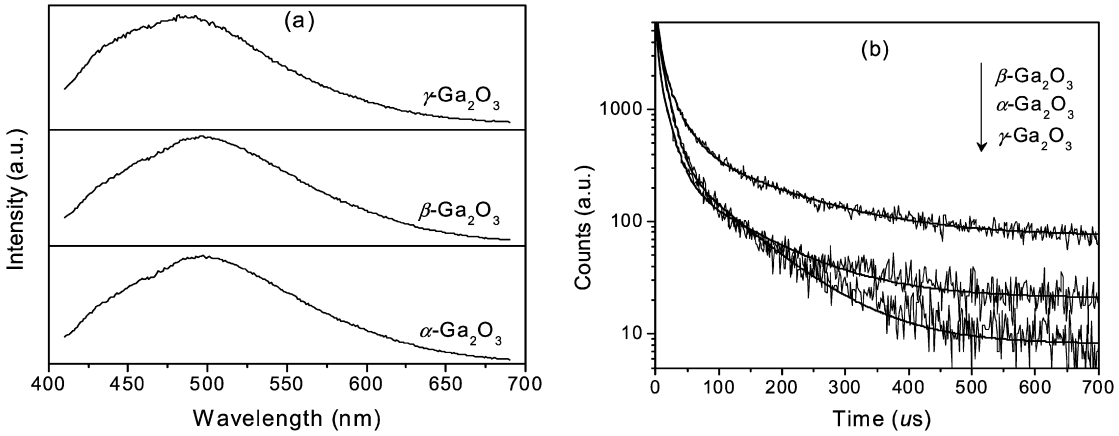

Fig. 4. Steady-state PL spectra (a) and PL decay curves (b) of the Ga_2O_3 polymorphs.

Table 2
The PL decay parameters of the Ga_2O_3 polymorphs measured at $\lambda_{ex} = 254$ nm and $\lambda_{em} = 490$ nm

Sample	Decay times (μs) with relative amplitudes (%) in brackets		
	τ_1	τ_2	τ_3
α-Ga_2O_3	3.2 (28)	15 (43)	109 (29)
β-Ga_2O_3	5.8 (26)	24 (36)	142 (38)
γ-Ga_2O_3	2.9 (38)	13 (46)	89 (16)

Table 3
Comparison of specific reaction rates for the photodegradation of benzene, toluene, and ethylbenzene over the Ga_2O_3 polymorphs and TiO_2 (the catalytic data was obtained at 12 h in the reaction)

Sample	S_{BET} ($m^2\,g^{-1}$)	Hydrocarbon removal rate ($\mu mol\,h^{-1}\,m^{-2}$)			CO_2 production rate ($\mu mol\,h^{-1}\,m^{-2}$)		
		C_6H_6	C_7H_8	C_8H_{10}	C_6H_6	C_7H_8	C_8H_{10}
α-Ga_2O_3	58	0.32	0.46	0.31	1.7	1.3	1.2
β-Ga_2O_3	80	0.42	0.52	0.36	2.4	1.8	1.6
γ-Ga_2O_3	135	0.21	0.26	0.20	0.95	0.85	0.73
TiO_2	50	0.08	0.15	0.18	0.17	0.13	0.15

3.4. Reactivity

Photocatalytic oxidation of aromatic compounds in a dry air stream over the Ga_2O_3 polymorphs was carried out under room temperature and atmospheric pressure. No reaction proceeded in absence of a catalyst or in the dark. Figs. 5, 6, and 7 show the photocatalytic performance of the Ga_2O_3 catalysts toward the decomposition of benzene, toluene, and ethylbenzene, respectively. The photocatalytic performance of the Ga_2O_3 polymorphs was also compared with that of commercially available TiO_2 (i.e., Degussa P25), a reference catalyst. All of the Ga_2O_3 materials exhibited much better reactivity than the TiO_2. Among the Ga_2O_3 polymorphs, the efficiency of the hydrocarbon removal over Ga_2O_3 decreased in the following order: β-$Ga_2O_3 > \gamma$-$Ga_2O_3 > \alpha$-Ga_2O_3 (Figs. 5, 6, and 7). CO_2 production over the Ga_2O_3 polymorphs follows a similar sequence (i.e., β-$Ga_2O_3 > \gamma$-$Ga_2O_3 > \alpha$-Ga_2O_3) and exceeds that produced over TiO_2. The above activity data combined with the physicochemical properties of the Ga_2O_3 polymorphs shown in Table 1 indicate that the photocatalytic performance of the Ga_2O_3 polymorphs may be changed with the crystallinity, pore structure, and size of the photocatalysts. However, there seems to be no corresponding correlation between the physicochemical parameters and the photoactivity of the Ga_2O_3 polymorphs. To reveal the intrinsic activities of the Ga_2O_3 polymorphs, we calculated the specific hydrocarbon removal rate and CO_2 production rate (expressed in terms of $\mu mol\,h^{-1}\,m^{-2}$); the data are summarized in Table 3 for comparison purposes. β-Ga_2O_3 obviously exhibits the highest specific photocatalytic activity among the Ga_2O_3 polymorphs, with α-Ga_2O_3 the second-most photoactive form of Ga_2O_3. Moreover, the control experiments show that, unlike in TiO_2, humidity had no obvious effect on the photocatalytic performance of the Ga_2O_3 photocatalysts.

4. Discussion

Because realization of the photoinduced processes in the Ga_2O_3 intrinsic absorption band requires irradiation with short-UV light, we used bactericidal lamps (emission wavelength 254 nm) to supply the excitation light in our experiments. Aromatic compounds also absorb light under such experimental conditions, making this photochemical process even more complicated. In the case of benzene, although benzene has a fine-structure absorption band centered at 254 nm [32], direct degradation was not observed in absence of the photocatalyst. To get more detailed information on the reaction mechanism, we also investigated the photodegradation of benzene over the dielectric oxides (e.g., Al_2O_3, SiO_2, MgO) and zeolite (e.g., ZSM-5). The results, given in Table 4, indicate that the photoinduced reaction occurs at the solid–gas interface. Such a photochemical reaction over wide-band-gap oxides originates from the existence of strong acceptor or donor sites typical for many oxide catalysts with pronounced acidic or basic properties and is known as "photochemistry of adsorbed species" [33]. However, the photoinduced reaction efficiency of benzene over wide-band-gap oxides is very low compared with that of Ga_2O_3, as shown in Tables 3 and 4. Therefore, the degradation of organic compounds over Ga_2O_3 observed in our experiment is attributed mainly to semiconductor photocatalysis rather than to "photochemistry of adsorbed species."

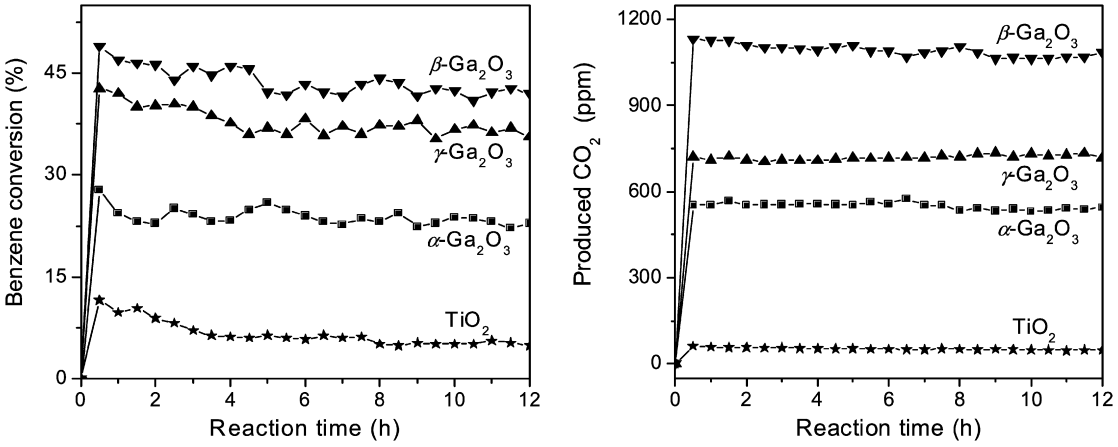

Fig. 5. Photocatalytic conversion of benzene and production of CO_2 over the Ga_2O_3 polymorphs and TiO_2 as a function of time on stream.

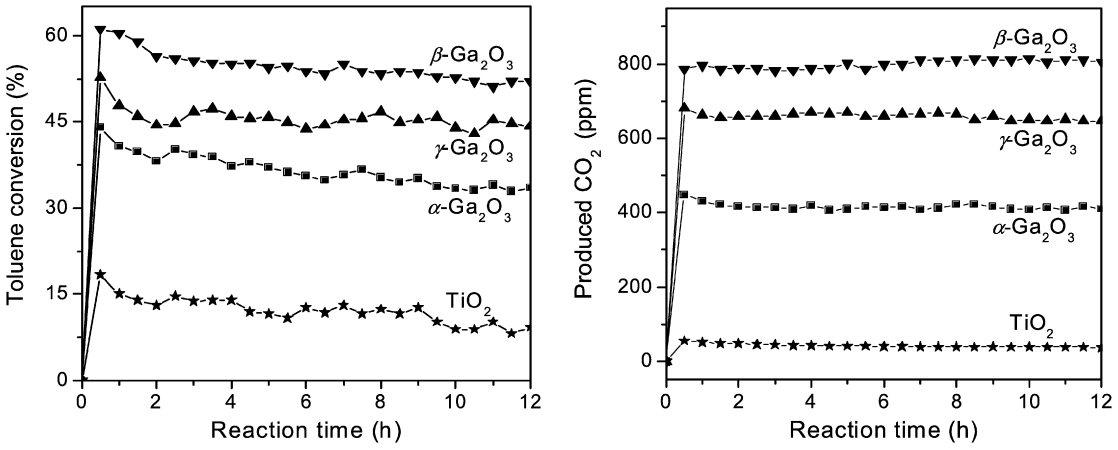

Fig. 6. Photocatalytic conversion of toluene and production of CO_2 over the Ga_2O_3 polymorphs and TiO_2 as a function of time on stream.

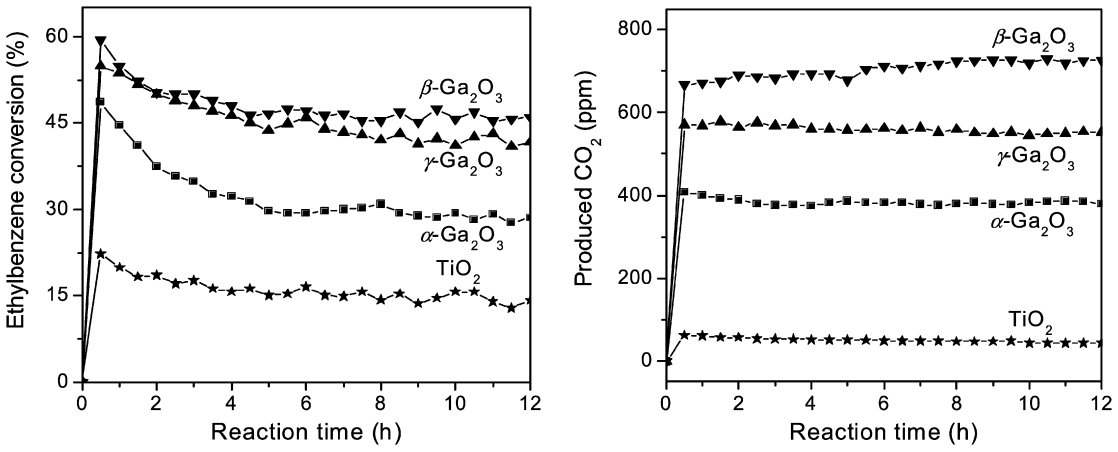

Fig. 7. Photocatalytic conversion of ethylbenzene and production of CO_2 over the Ga_2O_3 polymorphs and TiO_2 as a function of time on stream.

During the photocatalytic decomposition of aromatic compounds under UV illumination, the conversion and the amount of CO_2 produced over Ga_2O_3 are much higher than those over TiO_2. This might be associated with the band-gap structure of the photocatalysts. The conduction and valence bands of TiO_2 are composed of Ti $3d$ and O $2p$ orbitals, respectively. In the case of Ga_2O_3 containing Ga^{3+} with d^{10} electronic configuration, the valence band consists of O $2p$ orbitals, whereas the conduction band is composed of hybridized Ga $4s4p$ orbitals. The band-gap energy for Ga_2O_3 is 4.5–4.7 eV, much wider than the 3.2 eV for TiO_2. As a result, the photogenerated holes and electrons on Ga_2O_3 have stronger redox ability than those generated on TiO_2 [34]. This is beneficial for the destruction of stable reaction intermediates on Ga_2O_3 and the maintenance of a clean surface on the photocatalyst. As the photocatalytic reactions occur on the surface of catalyst, the

Table 4
Comparison of surface area and photocatalytic performance of Al_2O_3, SiO_2, MgO and ZSM-5 (the catalytic data was obtained at 12 h in the degradation reaction of benzene)

Sample	S_{BET} ($m^2\,g^{-1}$)	Benzene conversion (%)	Benzene removal rate ($\mu mol\,h^{-1}\,m^{-2}$)	CO_2 production (ppm)	CO_2 production rate ($\mu mol\,h^{-1}\,m^{-2}$)
Al_2O_3	199	3.7	0.015	22	0.019
SiO_2	480	5.3	0.009	26	0.01
MgO	50	2.5	0.04	23	0.082
ZSM-5	331	4.2	0.01	11	0.006

clean surface is favorable for gas–solid heterogeneous photocatalysis [35]. In addition, the photogenerated electron in *sp* hybridized band (Ga $4s4p$) has high mobility due to large band dispersion. Higher mobility of photogenerated electrons will improve the separation efficiency of the photogenerated holes and electrons. In this regard, new photocatalysts containing *p*-block metal cations with d^{10} electronic configuration (e.g., Ga^{3+}, Ge^{4+}, In^{3+}, Sn^{4+}, and Sb^{5+}) have been developed recently [36–38]. The valence band of these types of materials is composed mainly of hybridized *sp* orbitals with large band dispersion.

Among the Ga_2O_3 polymorphs, a difference in band-gap energy exists. The band-gap energy follows the sequence β-$Ga_2O_3 \approx \gamma$-$Ga_2O_3 > \alpha$-Ga_2O_3. Although β-Ga_2O_3 indeed seems to be the most efficient photocatalyst among the Ga_2O_3 polymorphs, the trend expected purely from the band-gap energies does not explain the experimental activity. The crystallinity of a photocatalyst has an important effect on its photocatalytic performance [39]. γ-Ga_2O_3 contains many and varied structural defects because of its low crystallinity. These defects are usually considered to act as recombination centers of the photogenerated electrons and holes, resulting in low separation efficiency of these couples [39]. This is confirmed by the time-resolved PL measurements. A longer PL lifetime means a more stable trapped electron–hole pair. During photocatalytic processes, the interfacial electron transfer of the trapped electron–hole pairs is the slowest step, and thus this step is the rate-limiting step for heterogeneous photocatalysis [35]. The higher recombination rate of the electron–hole pairs due to the low crystallinity seems to be the reason why γ-Ga_2O_3 has lower photocatalytic activity for the decomposition of hydrocarbons. An increased lifetime of photogenerated carriers from improved crystallinity is expected to result in higher quantum efficiency. Indeed, the prepared α-Ga_2O_3 and β-Ga_2O_3 have higher crystallinity, and, consequently, longer lifetimes of their electron–hole pairs on UV illumination. Therefore, they exhibit higher quantum efficiency than γ-Ga_2O_3.

The geometric and electronic structures of photocatalysts also greatly influence their photocatalytic activity [40–43]. The difference in reactivity among the Ga_2O_3 polymorphs might be related to their geometric and electronic structures. Using the crystallographic data regarding the atom positions, we have calculated the center of gravity of oxygen ions surrounding a Ga^{3+} ion for α-Ga_2O_3 and β-Ga_2O_3. Unfortunately, such crystallographic data are unavailable for γ-Ga_2O_3. The calcu-

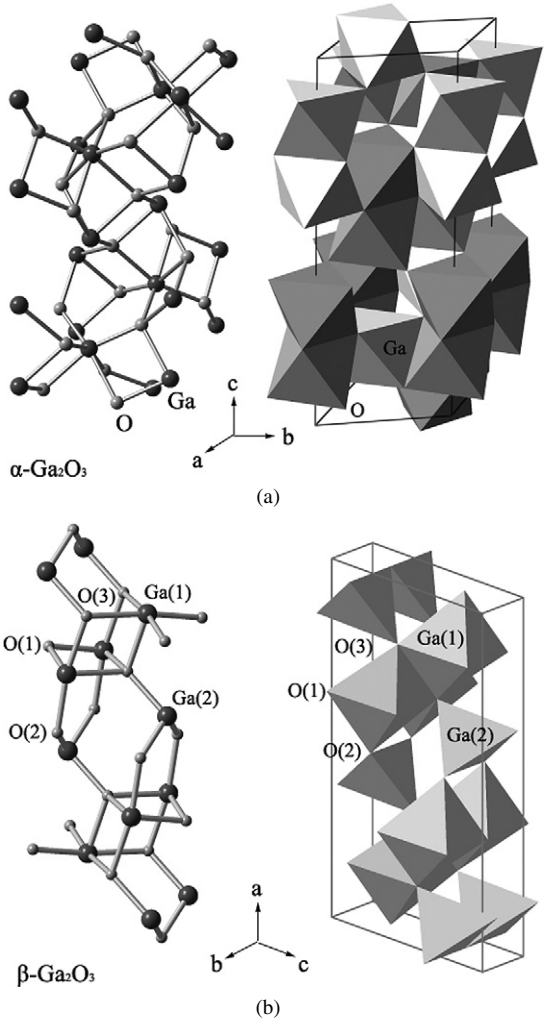

Fig. 8. Three-dimensional crystal structure of α-Ga_2O_3 (a) and β-Ga_2O_3 (b) with a unit cell.

lations show that α-Ga_2O_3 is constituted only by octahedral Ga^{3+} (Fig. 8a) and has a dipole moment of 4.2D inside the octahedron. For β-Ga_2O_3, GaO_6 octahedron and GaO_4 tetrahedron (Fig. 8b) coexist, both of which are so heavily distorted that the center of the gravity deviates from the position of the Ga^{3+} ion, generating dipole moments in the tetrahedral and octahedral units. For the two kinds of dipole moments, one inside the octahedron is 2.2D, and the other inside the tetrahedron is 0.7D. It is known that dipole moment induces the formation of local fields in the interior of the distorted polyhedra. The fields are considered to have functions promoting the separation of electron–hole pairs generated by light-irradiation of semiconductors [42]. A good correlation between the photocatalytic activity and the dipole moment (local fields) has been demonstrated [40]. For instance, MIn_2O_4 ($M = Ca^{2+}$, Sr^{2+}), consisting of distorted InO_6 octahedra with dipole moment, showed high photoactivity, whereas distortion-free $MInO_2$ (M = Li, Na) was negligibly active [40,41]. The study of MGa_2O_4 (M = Mg, Ca, Sr) also revealed that the distorted tetrahedra were associated with the photocatalytic activity. These findings indicate that the photocatalytic activity was extremely low for $MgGa_2O_4$ with normal octahedral GaO_6

but high for $SrGa_2O_4$ and $BaGa_2O_4$ with distorted tetrahedral units [40,42]. In the case of $BaTi_4O_9$ and $A_2Ti_6O_{13}$ (A = Na, K, Rb), comprising distorted TiO_6 octahedra of tunnel structure, TiO_6 octahedra promoted the formation of photoexcited charges functioning as active radicals in photocatalysis [44]. In summary, the activity of a photocatalyst is strongly associated with the distorted tetrahedral and octahedral units in the crystal structure of the catalyst [42]. In the case of β-Ga_2O_3, distorted tetrahedral and octahedral units coexist, resulting in the local internal fields. The coexistence of the two different kinds of fields might have synergic effects that promote the separation of photoexcited electron–hole pairs. In fact, the lifetime of photogenerated electron–hole pairs on β-Ga_2O_3 is longer than that on α-Ga_2O_3, as confirmed by the time-resolved PL measurements. This will partially contribute to the higher photocatalytic activity of β-Ga_2O_3 compared with α-Ga_2O_3.

5. Conclusion

In this study, we prepared three polymorphs of Ga_2O_3. In comparison with TiO_2, the Ga_2O_3 showed superior photocatalytic activity toward degradation of aromatic compounds in a dry air stream. Among the polymorphs, β-Ga_2O_3 exhibited the highest specific photocatalytic activity. The time-resolved PL data showed that the photogenerated carriers of β-Ga_2O_3 on illumination were the most stable, which promoted the photocatalytic oxidation reactions. The better photocatalytic performance of β-Ga_2O_3 was attributed to its good crystallinity and distorted geometric structure. Our findings may provide some insight into photocatalysis of the polymorph semiconductors.

Acknowledgments

This work was supported by the National Natural Science Foundation of China (grants 20537010, 20573020, 20571015, 20677009, and 20603007), the 973 Project (grant 2006CB7086-05), and grants from Fujian Province (E0510011, 2006J0160, and 2005HZ1008). The authors thank Professor H.H. Zhang and Mrs. R.Q. Sun for experiments and discussion of the PL measurements.

References

[1] Q. Lan, L. Zhang, G. Li, R. Vermeulen, R.S. Weinberg, M. Dosemeci, S.M. Rappaport, M. Shen, B.P. Alter, Y. Wu, W. Kopp, S. Waidyanatha, C. Rabkin, W. Guo, S. Chanock, R.B. Hayes, M. Linet, S. Kim, S. Yin, N. Rothman, M.T. Smith, Science 306 (2004) 1774.
[2] D.F. Ollis, C.Y. Hsiao, L. Budiman, C.L. Lee, J. Catal. 88 (1984) 89.
[3] R.W. Matthews, J. Catal. 97 (1986) 565.
[4] M.A. Fox, M.T. Dulay, Chem. Rev. 93 (1993) 341.
[5] S.A. Larson, J.L. Falconer, Catal. Lett. 44 (1997) 57.
[6] H. Einaga, S. Futamura, T. Ibusuki, Appl. Catal. B Environ. 38 (2002) 215.
[7] H. Einaga, S. Futamura, T. Ibusuki, Phys. Chem. Chem. Phys. 1 (1999) 4903.
[8] H. Einaga, S. Futamura, T. Ibusuki, Environ. Sci. Technol. 35 (2001) 1880.
[9] X.Z. Fu, W.A. Zeltner, M.C. Anderson, Appl. Catal. B Environ. 6 (1995) 209.
[10] C. Belver, M.J. López-Muñoz, J.M. Coronado, J. Soria, Appl. Catal. B Environ. 46 (2003) 497.
[11] H. Einaga, T. Ibusuki, S. Futamura, Environ. Sci. Technol. 38 (2004) 285.
[12] Y.L. Chen, D.Z. Li, X.C. Wang, X.X. Wang, X.Z. Fu, Chem. Commun. (2004) 2304.
[13] Y.D. Hou, X.C. Wang, L. Wu, Z.X. Ding, X.Z. Fu, Environ. Sci. Technol. 40 (2006) 5799.
[14] C.Y. Wu, X.P. Zhao, Y.J. Ren, Y.H. Yue, W.M. Hua, Y. Cao, Y. Tang, Z. Gao, J. Mol. Catal. A Chem. 229 (2005) 233.
[15] A.L. Linsebigler, G. Lu, J.T. Yates, Chem. Rev. 95 (1995) 735.
[16] A. Sclafani, J.M. Herrmann, J. Phys. Chem. 100 (1996) 13655.
[17] A. Kudo, K. Omori, H. Kato, J. Am. Chem. Soc. 121 (1999) 11459.
[18] R. Roy, V.G. Hill, E.F. Osborn, J. Am. Chem. Soc. 74 (1952) 719.
[19] B. Zheng, W.M. Hua, Y.H. Yue, Z. Gao, J. Catal. 232 (2005) 143.
[20] S.E. Collins, M.A. Baltanas, A.L. Bonivardi, Langmuir 21 (2005) 962.
[21] S.E. Collins, M.A. Baltanas, A.L. Bonivardi, J. Phys. Chem. B 110 (2006) 5498.
[22] C.O. Areán, A.L. Bellan, M.P. Mentruit, M.R. Delgado, G.T. Palomino, Micropor. Mesopor. Mater. 40 (2000) 35.
[23] D. Machon, P.F. McMillan, B. Xu, J. Dong, Phys. Rev. B 73 (2006) 094125.
[24] H.H. Tippins, Phys. Rev. A 140 (1965) A316.
[25] H.G. Kim, W.T. Kim, J. Appl. Phys. 62 (1987) 2000.
[26] N. Ueda, H. Hosono, R. Waseda, H. Kawazoe, Appl. Phys. Lett. 71 (1997) 933.
[27] Y.N. Xu, W.Y. Ching, Phys. Rev. B 44 (1991) 11048.
[28] D.M. Christie, J.R. Chelikowsky, Phys. Rev. B 62 (2000) 14703.
[29] T. Harwig, F. Kellendonk, J. Solid State Chem. 24 (1978) 255.
[30] L. Binet, D. Gourier, J. Phys. Chem. Solids 59 (1998) 1241.
[31] C.H. Liang, G.W. Meng, G.Z. Wang, L.D. Zhang, S.Y. Zhang, Appl. Phys. Lett. 78 (2001) 3202.
[32] V.M. Parikh, Absorption Spectroscopy of Organic Molecules, Addison–Wesley, Reading, MA, 1974.
[33] A.M. Volodin, Catal. Today 58 (2000) 103.
[34] Y. Xu, M.A.A. Schoonen, Am. Mineral. 85 (2000) 543.
[35] M.R. Hoffmann, S.T. Martin, W. Choi, D.W. Bahnemann, Chem. Rev. 95 (1995) 69.
[36] K. Ikarashi, J. Sato, H. Kobayashi, N. Saito, H. Nishiyama, Y. Inoue, J. Phys. Chem. B 106 (2002) 9048.
[37] J. Sato, H. Kobayashi, K. Ikarashi, N. Saito, H. Nishiyama, Y. Inoue, J. Phys. Chem. B 108 (2004) 4369.
[38] J. Sato, N. Saito, H. Nishiyama, Y. Inoue, J. Phys. Chem. B 105 (2001) 6061.
[39] M. Toyoda, Y. Nanbu, Y. Nakazawa, M. Hirano, M. Inagaki, Appl. Catal. B Environ. 49 (2004) 227.
[40] J. Sato, S. Saito, H. Nishiyama, Y. Inoue, J. Phys. Chem. B 107 (2003) 7965.
[41] J. Sato, H. Kobayashi, N. Saito, H. Nishiyama, Y. Inoue, J. Photochem. Photobiol. A Chem. 158 (2003) 139.
[42] J. Sato, H. Kobayashi, Y. Inoue, J. Phys. Chem. B 107 (2003) 7970.
[43] J. Sato, N. Saito, H. Nishiyama, Y. Inoue, J. Photochem. Photobiol. A Chem. 148 (2002) 85.
[44] M. Kohno, S. Ogura, K. Sato, Y. Inoue, J. Chem. Soc. Faraday Trans. 93 (1997) 2433.